JOURNAL OF COMPUTATIONAL PHYSICS 120, 231–247 (1995)

The Darwin Direct Implicit Particle-in-Cell (DADIPIC) Method for Simulation of Low Frequency Plasma Phenomena*

MATTHEW R. GIBBONS AND DENNIS W. HEWETT

Plasma Physics Research Institute, Lawrence Livermore National Laboratory, Livermore, California 94550

Received September 2, 1994; revised February 1, 1995

We describe a new algorithm for simulating low frequency, kinetic phenomena in plasmas. Darwin direct implicit particle-in-cell (DADIPIC), as its name implies, is a combination of the Darwin and direct implicit methods. Through the Darwin method the hyperbolic Maxwell's equations are reformulated into a set of elliptic equations. Propagating light waves do not exist in the formulation so the Courant constraint on the time step is eliminated. The direct implicit method is applied only to the electrostatic field with the result that electrostatic plasma oscillations do not have to be resolved for stability. With the elimination of these constraints spatial and temporal discretization can be much larger than that possible with explicit, electrodynamic PIC. We discuss the algorithms for pushing the particles and solving for the fields in 2D cartesian geometry. We also detail boundary conditions for conductors and dielectrics. Finally, we present two test cases, electron cyclotron waves and collisionless heating in inductively coupled plasmas. For these test cases DADIPIC shows agreement with analytic kinetic theory and good energy conservation characteristics.

I. INTRODUCTION

We have developed a new algorithm, the Darwin direct implicit particle-in-cell (DADIPIC) method, to simulate kinetic, low frequency phenomena in plasmas. We have found that this algorithm, which combines the features of direct implicit PIC [1] with the streamline Darwin field method [2], provides a flexible, robust alternative to the implicit, fully electromagnetic field models. We have implemented DADIPIC in a code which functions in a two-dimensional x–z region with all three components of the particle velocities, the electric field, and the magnetic field. Internal structures in the simulation region may be conductors or dielectrics, can be set at desired potentials, and driven with specified currents.

Before delving into the specifics of DADIPIC, a review of particle simulation of plasmas will provide a basis for discussion of the differences, advantages, and limitations of the new algorithm compared to other plasma simulation methods. Since plasma phenomena in many cases involve nonlinear effects and requires boundaries which are not amenable to analytic solutions, computer codes are invaluable in the simulation of plasma. Particle-in-cell (PIC) simulation is a proven way kinetically modeling the kinetic behaviour of a plasma with a number of simulation particles. Each particle has its own position, $\mathbf{x}$, and velocity, $\mathbf{v}$, which change according to the electromagnetic forces on the particles. The field quantities, $\mathbf{E}$, and $\mathbf{B}$, are stored on the grid and are advanced according to Maxwell's equations.

The typical time cycle has the following four steps: (1) interpolate fields from the grid to the particles to find the particle forces, (2) integrate the particle equations of motion, (3) interpolate particle quantities to the grid to find the field sources, and (4) integrate the field equations using these source terms. The main differences between PIC codes come down to methods of integrating the particle equations of motion, methods of solving for the fields, interpolation of particle and field quantities, and boundary conditions. The choice of methods is driven by the need to retain only the plasma properties contributing to the phenomena being studied.

The most straightforward and the computationally quickest individual time step simply involves the explicit finite difference formulation of the equations of motion and Maxwell's equations. This provides a way to carry out the time advance of the particles and fields in steps (2) and (4) of the time cycle. With this explicit formulation we ratain all of the electromagnetic and course-grain kinetic behaviour of the plasma. However, as with any finite difference advance of a hyperbolic set of equations, we run into constraints on the spacial and temporal discretization in order to avoid instability, $c\Delta x/\Delta t < 1$ and $\omega_{pe}\Delta t < 2$.

0021-9991/95 $12.00

A. Low Frequency, Kinetic Phenomena

One of the difficulties in simulating plasmas lies in the enormous disparity between the fundamental scale lengths of a plasma and the scale lengths of the phenomena of interest. The fundamental parameters involve the Debye length, the plasma frequency, and the propagation time of electromagnetic waves. Reduced physics models such as fluid algorithms would allow the computationalist to ignore the constraints imposed by these fundamental parameters, but in many cases the kinetic properties of the plasma are intimately involved in the transport of energy and particles. Explicit electrodynamic PIC would correctly model this physics, but the discretization in space and time required due to the constraints on the algorithm is often prohibitive. The problems can easily demand more storage and speed than present computers can provide.

The objective becomes to create models which can ignore the fundamental constraints without eliminating relevant plasma properties. Properties to retain include: kinetic effects such as collisionless damping of low frequency waves and nonanalytic particle velocity distributions, electrostatic as well as magnetoinductive fields, finite electron mass effects, and nonlinear processes.

Two examples of low frequency, kinetic phenomena are magnetic reconnection and plasma processing. Magnetic reconnection is, as its name implies, the breaking and reconnection of magnetic field lines in resistive media. This process itself exists over a wide range of spacial and temporal scale lengths in astrophysical, geophysical, and magnetic fusion plasmas [3]. It is considered important in the transport processes of these plasmas and can depend on the ion and electron velocity distributions. Fluid descriptions of the phenomena require empirical additions to the equations which are not consistent with the known properties of the plasmas. Kinetic simulations remain the best way to study magnetic reconnection, even though it may occur over widths of tens of Debye lengths and times equal to $1000\omega_{pe}^{-1}$.

Plasma processing is an important application of plasmas where boundaries need to be considered. Plasma processing involves the use of plasmas in the treating of material surfaces for microelectronic and other industries. There are various ways of generating the plasma. Among these are inductive reactors which excite the plasma with inductive fields operating at frequencies near 10 MHz with sufficient power to generate plasma densities of $n_p = 10^{11}$ cm^{-3} [4]. Typical sizes of these reactors are $L = 10$ cm. This results in parameters of $L > \Delta x = 0.1$ cm $\gg \lambda_{De} = 0.005$ cm and $c/\Delta x = 3 \times 10^{11}$ s$^{-1} > \omega_{pe} = 2 \times 10^{10}$ s$^{-1} \gg \omega_{rf}$. Since electron collisions are a main source of ionization and other chemical reactions in the chamber, the electron velocity distribution has a major impact on the reactor operation. Because the inductive fields cause heating through both resistive and collisionless processes, the distribution need not be Maxwellian.

B. Long Time Scale Simulation Methods

Over the past 20 years several PIC methods have been developed to overcome the constraints on explicit electrodynamic PIC. These methods eliminate selected high frequency plasma phenomena while retaining long time-scale, kinetic phenomena. The approaches can be split into two broad categories according to the way they remove the high frequency, short wavelength phenomena. The first category works with the original set of equations and reduces the physics. The set of equations is no longer hyperbolic for certain sets of waves (usually light waves and plasma oscillations). The second category works with the finite difference equations in an implicit form. All of the waves still exist in the simulation but those which are not resolved are numerically damped out.

1. *Physics Reduction Methods*

The Darwin method is the minimum reduction in Maxwell's equations necessary to eliminate the propagation of light waves [5, 6]. The essence of this radiation free limit is obtained by ignoring the solenoidal part of the displacement current in Ampere's law. This results in a particle Lagrangian which is correct to order v^2/c^2. The set of Darwin equations can be rewritten in elliptic form. Section II.B will elaborate on the form of the equations and their numerical solution.

Significant progress has been made in the numerical implementation of Darwin for PIC codes. The initial Darwin algorithms decomposed the plasma source terms into an irrotational, or curl free, part and a solenoidal, or divergence free, part in order to solve the partial differential equation for the B-field and solenoidal E-field [6]. This process was both numerically time consuming and conceptually daunting. In many cases the boundary conditions needed to solve for the irrotational and solenoidal parts of the plasma source terms are beyond the physical insight of the investigator. The derivation of the streamlined Darwin field (SDF) equations by Hewett and Boyd removed the need for a decomposition and reformulated the equation with variables which require relatively simple boundary conditions [2]. However, SDF consists of two strongly coupled partial differential equations. The linear system due to the finite differencing of these equations was found to be difficult to solve. This problem was overcome with the extension of the iterative matrix solution technique dynamic alternating direction implicit (DADI) to coupled equations [7].

With these improvements the Darwin equations can be solved quickly and efficiently in a plasma simulation code. The method eliminates the CFL constraint on light propagation while retaining all kinetic effects for the particles in the radiation free fields. The Darwin field equations reduce the size of electromagnetic fluctuations compared to fully electromagnetic codes [6]. This allows the use of fewer particles resulting in a further increase in computational speed beyond the use of a larger time step. Unfortunately, for higher density plasmas the constraint due to ω_{pe} can be almost as restrictive as the CFL condition.

2. *Implicit Methods*

Implicit methods achieve stability by including information from the next time step in the equations for the time advance

of present quantities. Contributions from previous time steps may also be retained depending on the amount of numerical dispersion which is desired or tolerable. If all quantities are stored on the same grid and the dynamic equations depend on the local values of grid quantities, the implicit system can be formulated into a set of simultaneous equations. The solution of the simultaneous equations gives the grid quantities at the next time step.

For PIC simulation the situation is more complicated. The particles have positions and velocities independent of the grid, and the field equations can be elliptic requiring global solutions much more involved than a simple relationship to local grid quantities. For this reason the methods used are actually predictor–corrector. The source terms (usually ρ and $\mathbf{J}$) are found at an intermediate level using the present field values. Equations for the time advanced fields are derived by expanding the normal field equations around the arguments at the intermediate level [8]. Truncating the expansion gives approximate equations for the time advanced fields in terms of the present fields and the intermediate level sources. The particles are then pushed to the next time step by using the time advanced fields. The estimated fields are not necessarily consistent with final particle positions and velocities. In principle iterations over the above steps could be done to improve convergence, but this has not been found to be necessary [8]. If one did iterate to convergence, the methods would be truly implicit. The two approaches to implicit PIC, the moment method and the direct method, differ primarily in how the source terms are advanced to the intermediate level.

In the moment method the source terms to be advanced are the fluid quantities which have been interpolated to the grid from the particles. The moment of fluid equations are used to give the time variation of these quantities, and the terms in the fluid equations are found from additional accumulations of particle quantities. The fluid quantities are then advanced to the intermediate level through a finite difference of the time derivatives, where the numerical accuracy of advection schemes can play a role. Initial work with electrostatic codes can be found in Mason [9] and Denavit [10]. Overviews of moment method electromagnetic algorithms are in Brackbill and Forslund [11] and Mason [12].

The direct method avoids the inconsistencies of taking moments by continuing to work directly with the particles. Both the particle positions and velocities are moved to the intermediate level. The particle quantities are then interpolated to the grid to provide the source terms for the implicit field equations. This leads to a double push and interpolation of the particle quantities. Since dealing with the particles can take most of the cpu time, a computational cost is paid for the greater accuracy of working directly with the particles. Dispersion characteristics and grid effects have been thoroughly investigated in several sources [1, 13]. An overview of the method including electromagnetics and energy conservation characteristics can be found in Langdon and Barnes [8]. Hewett and Langdon [14] and Tanaka [15] provide results from fully electromagnetic implicit codes.

These implicit methods provide plasma simulation with large temporal and spatial discretization while retaining electron kinetics. The strength of the implicit scheme is that those phenomena which are not resolved are numerically damped. This becomes a constraint when the numerical dispersion cooling effects and grid heating effects cause significant numerical changes in total system energy. Energy conservation is achieved only if Δx and Δt are chosen correctly [14, 16]. The other limitation to these methods has been finding reasonable boundary conditions for the implicit electromagnetic fields.

3. *The Darwin Direct Implicit (DADIPIC) Method*

As its name suggests DADIPIC is a combination of the Darwin and direct implicit methods. The direct implicit algorithm is used only to solve for an implicit electrostatic field. The SDF equations are used to solve for the solenoidal E-field and the B-field. The particles are advanced explicitly in time with respect to the solenoidal E-field and the B-field. As will be shown in the remainder of this paper, DADIPIC combines the previously mentioned useful features of these two methods while eliminating or at least mitigating their constraints. Darwin is no longer limited by $\omega_{pe}\Delta t$ because of the electrostatic direct implicit particle advance. Boundary conditions are much simpler since they are applied separately to the implicit electrostatic field and the SDF equations. The issue of energy nonconservation also appears to be manageable since fluctuations due to the electrostatic field are the only culprits.

In the remainder of this paper we present the DADIPIC algorithm and some tests of its performance. Section II.A covers the direct implicit, electrostatic method in the presence of electromagnetic fields. We discuss the Darwin method in Section II.B and dielectrics in II.C. The steps in the particle integrations and field solution for the combined algorithm are in Section II.D. Section III contains the results of the application of DADIPIC to electron cyclotron waves and collisionless heating in inductively coupled plasmas.

II. IMPLEMENTATION OF DARWIN DIRECT IMPLICIT PARTICLE-IN-CELL

Our implementation of DADIPIC results in an algorithm in which the implicit electrostatic step and the Darwin step each stand alone. So we will describe the implementation of each step separately before presenting the combined algorithm.

A. Implicit Electrostatic Method

In this section we describe the particle advance and field solve necessary to carry out the implicit electrostatic part of the DADIPIC algorithm.

1. *Particle Integration*

The particles are time integrated according to the D1 implicit scheme [1]. This scheme damps high frequency oscillations while retaining low frequency oscillations by keeping significant contributions from all previous time steps in the electrostatic part of the particle acceleration. The D1 scheme also extends the region of energy conservation in $\Delta x/\lambda_{De}$, $\omega_{pe}\Delta t$ space as compared to the more time centered C1 scheme [16]. In fact good energy conservation for the D1 scheme was found when $3v_{th}\Delta t/\Delta x \sim 1$. The finite differenced equations take the form

$$\begin{aligned}
\mathbf{v}^{n+1/2} &= \mathbf{v}^{n-1/2} + \Delta t\bar{\mathbf{a}}^n + \frac{q\Delta t}{m}\left[\mathbf{E}^n_{\text{sol}} + \frac{\mathbf{v}^{n+1/2} + \mathbf{v}^{n-1/2}}{2c} \times \mathbf{B}^n\right] \\
\mathbf{x}^{n+1} &= \mathbf{x}^n + \Delta t\mathbf{v}^{n+1/2} \\
\bar{\mathbf{a}}^n &= \frac{1}{2}\left[\bar{\mathbf{a}}^{n-1} + \frac{q}{m}\mathbf{E}^{n+1}_{\text{irr}}\right],
\end{aligned} \tag{2.1}$$

where $\mathbf{E}_{\text{sol}}$ is the solenoidal part of the field and $\mathbf{E}_{\text{irr}}$ is the irrotational part of the field. Note that $\bar{\mathbf{a}}$ carries only the time advanced electrostatic field. Unlike other electromagnetic implicit algorithms, the particle push is still explicit with respect to $\mathbf{E}_{\text{sol}}$ and $\mathbf{B}$. So a time advanced field solve must only be found for $\mathbf{E}_{\text{irr}}$. This particle push is broken up into two steps [14]. The first push uses only known quantities to advance $\mathbf{v}$ and $\mathbf{x}$ to a $\sim$ level, and the $\sim$ quantities are used to estimate the advanced $\mathbf{E}_{\text{irr}}$. The predicted $\mathbf{E}_{\text{irr}}$ is then used to complete the advance to the $n + 1$ time step. As mentioned above the method is a predictor–corrector as opposed to truly implicit.

In these equations the interpolation from particles to the grid and vice versa is accomplished through shape functions. The effects of these functions on the simulation have been extensively discussed [17]. The form of the function is $S(\mathbf{x}_j - \mathbf{x}_i)$, where $\mathbf{x}_j$ is a grid node coordinate and $\mathbf{x}_i$ is a particle position. For this code linear shape functions have been used with the form

$$S(\mathbf{x}_j - \mathbf{x}_i) = (x_j + \Delta x - x_i)(z_j + \Delta z - z_i)/\Delta x\,\Delta z. \tag{2.2}$$

Equation (2.2) is for a particle in a cell located in the positive x and z directions with respect to the grid node. The other nodes of a cell have similar functions. The sources for the field equations on the grid are obtained by sums over the particles in a particular cell of the appropriate particle quantity multiplied by the shape function. As an example the charge density is

$$\rho_j = \frac{1}{\Delta x\,\Delta z}\sum_i q_i S(\mathbf{x}_j - \mathbf{x}_i). \tag{2.3}$$

Note that Eq. (2.1) is implicit with respect to the velocity. This equation can be reformulated so that the advanced velocity is exclusively on the left-hand side [18]. Using tensor notation the equation becomes

$$\mathbf{v}^{n+1/2} = \mathbf{R}^n \cdot \mathbf{v}^{n-1/2} + \frac{\Delta t}{2}(\mathbf{I} + \mathbf{R}^n) \cdot \left(\bar{\mathbf{a}}^n + \frac{q}{m}\mathbf{E}^n_{\text{sol}}\right), \tag{2.4}$$

where $\mathbf{I}$ is the identity tensor and $\mathbf{R}$, the rotation due to $\mathbf{v} \times \mathbf{B}$, is given by

$$\begin{aligned}
\mathbf{R}^n &= [(1 - (\Theta^n)^2)\mathbf{I} - 2\Theta^n \times \mathbf{I} + 2\Theta^n\Theta^n]/(1 + (\Theta^n)^2) \\
\Theta^n &= q\mathbf{B}^n\Delta t/2mc.
\end{aligned} \tag{2.5}$$

Using the notation of Eq. (2.5), we obtain

$$\begin{aligned}
\tilde{\mathbf{v}} &= \mathbf{R}^n \cdot \mathbf{v}^{n-1/2} + \frac{\Delta t}{2}(\mathbf{I} + \mathbf{R}^n) \cdot \left(\frac{1}{2}\bar{\mathbf{a}}^n + \frac{q}{m}\mathbf{E}^n_{\text{sol}}\right) \\
\tilde{\mathbf{x}} &= \mathbf{x}^n + \Delta t\tilde{\mathbf{v}}.
\end{aligned} \tag{2.6}$$

The final positions and velocities are obtained from

$$\begin{aligned}
\mathbf{v}^{n+1/2} &= \tilde{\mathbf{v}} + \delta\mathbf{v} \\
\mathbf{x}^{n+1} &= \tilde{\mathbf{x}} + \Delta t\,\delta\mathbf{v} \\
\delta\mathbf{v}(\mathbf{x}^n, \mathbf{x}^{n+1}) &= \frac{q\Delta t}{4m}(\mathbf{I} + \mathbf{R}^n)\mathbf{E}^{n+1}_{\text{irr}}(\mathbf{x}^{n+1}).
\end{aligned} \tag{2.7}$$

Note that $\mathbf{R}$ should be evaluated at $\mathbf{x}^n$, and $\mathbf{E}_{\text{irr}}$ should be evaluated at $\mathbf{x}^{n+1}$ for $\delta\mathbf{v}$. With this scheme $\delta\mathbf{v}$ cannot be found until the advanced $\mathbf{E}_{\text{irr}}$ is estimated. An approximate field equation is obtained by taking the first two terms of a Taylor expansion of the accumulated charge density at time $n + 1$ about $\tilde{\mathbf{x}}$:

$$\rho^{n+1} = \sum_i \frac{q_i}{\Delta x}[S(\mathbf{x}_g - \tilde{\mathbf{x}}_i) + \Delta t\,\delta\mathbf{v}_i(\mathbf{x}_i^n, \mathbf{x}_i^{n+1}) \cdot \nabla_i S(\mathbf{x}_g - \tilde{\mathbf{x}}_i) + \ldots]. \tag{2.8}$$

Noting that the first term is $\tilde{\rho}$, Eq. (2.8) can be rewritten

$$\rho^{n+1} \simeq \tilde{\rho} + \sum_i \frac{q_i}{\Delta x}[\Delta t\,\delta\mathbf{v}_i(\mathbf{x}_i^n, \mathbf{x}_i^{n+1}) \cdot \nabla_i S(\mathbf{x}_g - \tilde{\mathbf{x}}_i)]. \tag{2.9}$$

In the second term the gradient can be changed to a derivative on the grid position and removed from the sum. Several methods of calculating the remaining sum have been investigated [13, 8]. One of the least computationally intensive and most stable has been termed simplified differencing [1]. In simplified differencing $\mathbf{R}$ and the E-field are evaluated on the grid leaving

TABLE I

Coefficients for the Implicit Field Equation Operator

$\phi_{i+1,j+1}$	dpp	$(1/4\ \Delta x\ \Delta z)(X^{13}_{i+1/2,j} + X^{31}_{i,j+1/2})$
$\phi_{i+1,j}$	cxp	$(1/\Delta x^2)(1 + X^{11}_{i+1/2,j})(1/4\ \Delta x\ \Delta z)(X^{31}_{i,j+1/2} - X^{31}_{i,j-1/2})$
$\phi_{i+1,j-1}$	dpm	$-(1/4\ \Delta x\ \Delta z)(X^{13}_{i+1/2,j} + X^{31}_{i,j-1/2})$
$\phi_{i,j+1}$	czp	$(1/\Delta z^2)(1 + X^{33}_{i,j+1/2})(1/4\ \Delta x\ \Delta z)(X^{13}_{i+1/2,j} - X^{13}_{i-1/2,j})$
$\phi_{i,j}$	ccc	$-2(1/\Delta x^2 + 1/\Delta z^2) - (1/\Delta x^2)(X^{11}_{i+1/2,j} + X^{11}_{i-1/2,j})$ $-(1/\Delta z^2)(X^{33}_{i,j+1/2} + X^{33}_{i,j-1/2})$
$\phi_{i,j-1}$	czm	$(1/\Delta z^2)(1 + X^{33}_{i,j-1/2}) - (1/4\ \Delta x\ \Delta z)(X^{13}_{i+1/2,j} - X^{13}_{i-1/2,j})$
$\phi_{i-1,j+1}$	dmp	$-(1/4\ \Delta x\ \Delta z)(X^{13}_{i-1/2,j} + X^{31}_{i,j+1/2})$
$\phi_{i-1,j}$	cxm	$(1/\Delta x^2)(1 + X^{11}_{i-1/2,j}) - (1/4\ \Delta x\ \Delta z)(X^{31}_{i,j+1/2} - X^{31}_{i,j-1/2})$
$\phi_{i-1,j-1}$	dmm	$(1/4\ \Delta x\ \Delta z)(X^{13}_{i-1/2,j} - X^{31}_{i,j-1/2})$

$$\rho^{n+1} = \tilde{\rho} - \nabla\cdot(\mathbf{X}\cdot\mathbf{E}^{n+1}_{\text{int}})$$
$$\mathbf{X}_g = \frac{\Delta t^2}{4}\sum_s (\mathbf{I} + \mathbf{R}^n_g)\left[\frac{q_s\tilde{\rho}_s}{m_s}\right], \tag{2.10}$$

where the sum is now over species. The **X** tensor is easily formed from the B-field and charge density already stored on the grid. This differencing provides a significant reduction in computation since it avoids extra interpolation of particle quantities to the grid and leads to a simpler finite difference field solution. For instance, in 1D the field solution goes from a pentadiagonal solution matrix with strict differencing to a tridiagonal solution matrix with simplified differencing. With the simplified differencing expression for ρ^{n+1} the field equation becomes

$$\nabla\cdot[(\mathbf{I} + 4\pi\mathbf{X})\cdot\nabla\phi^{n+1}] = -4\pi\tilde{\rho}. \tag{2.11}$$

Because of the similarity of this equation to the electrostatic field equation in dielectric media, the **X** term is usually referred to as an implicit susceptibility [1].

2. *Differencing of the Field Equation and Boundary Conditions*

Simplified differencing is implemented in the code as follows. In the x–z plane the implicit field equation has the form

$$[\nabla^2 + 4\pi(\nabla_x(X^{11}\nabla_x + X^{13}\nabla_z) + \nabla_z(X^{31}\nabla_x + X^{33}\nabla_z))]\phi_{n+1} = -4\pi\tilde{\rho}. \tag{2.12}$$

These terms are finite differenced with second-order accuracy as

$$\nabla_x(X^{11}\nabla_x\phi_{n+1}) = \frac{1}{(\Delta x)^2}[X^{11}_{i+1/2,j}\phi^{n+1}_{i+1,j} + X^{11}_{i-1/2,j}\phi^{n+1}_{i-1,j} - (X^{11}_{i+1/2,j} + X^{11}_{i-1/2,j})\phi^{n+1}_{i,j}] \tag{2.13}$$

with the other terms having similar expressions. This leads to a nine-point scheme of coefficients in the solution matrix, **A**, for each potential node to be solved. The resulting coefficients are in Table I. **A** is formed with $\phi(i, j)$ ordered in a 1D vector as $[\phi_{1,1}, \ldots, \phi_{i\ \max,1}, \phi_{1,2}, \ldots, \phi_i\ \phi_{i\ \max,2}, \ldots]$. **A** is a banded matrix, and to save on storage only the diagonals with nonzero components are stored by the code. Note that the components of the **X** tensor are needed at the half grid point positions. These are calculated by averaging the densities and B-fields which are stored at the grid points. As an example $X(i - \frac{1}{2}, j)$ generates its rotation tensor from the B-field: $B(i - \frac{1}{2}, j) = 0.5(B(i - 1, j) + B(i, j))$.

Periodic, Dirichlet, and Neumann boundary conditions on ϕ are allowed by the code. Periodic boundaries represent an infinite repetition of the simulation region along the periodic direction. Essentially there is no boundary only a limitation on maximum wavelength. For periodic boundaries, nodes outside one of the four bounding walls of the simulation region are the same as nodes just inside the opposite wall. This moves the coefficient for that node to a different diagonal in the solution matrix. As a result the number of diagonals changes for periodic boundary conditions (15 for periodic, 21 for doubly periodic). For Dirichlet nodes, such as a conductor where we want to set a specific potential, the coefficient on the diagonal is set to one, the other coefficients are set to zero, and the right-hand side is set to the value of ϕ desired for that node. For Neumann nodes exterior nodes required by the finite difference template are found from interior nodes according to

$$\phi_{i\,\max+1,j} = \phi_{i\,\max-1,j} + \Delta x\frac{\partial\phi}{\partial x}. \tag{2.14}$$

The exterior node coefficient is simply added to the interior node coefficient, and the derivative term is added to the right-hand side of the matrix equation. This condition is most commonly used along axes of symmetry, where $\partial\phi/\partial x$ is set to zero.

Once ϕ is calculated, the electric field must be found. For interior points the gradient of ϕ is used:

$$E^x_{i,j} = -(\phi_{i+1,j} - \phi_{i-1,j})/(2\Delta x). \tag{2.15}$$

Conducting boundaries present a unique situation. Under long time scale conditions a confined plasma will generally rise to a positive potential with respect to the confining walls. This potential drop retards the more mobile electrons and accelerates the heavier ions causing an equalization of the electron and ion currents being absorbed by the walls. The resulting potential sheath is typically large compared to a Debye length, but may be small compared to the region to be simulated. This leads us to use different boundary conditions at conducting boundaries depending on whether a sheath is spatially resolved or not.

When the sheath is resolved an implicit Gauss' law is used to overcome the lack of ϕ values exterior to the conducting boundary [19]. The integral form of the implicit field equation is

$$\int(\mathbf{I} + 4\pi\mathbf{X})\mathbf{E}\cdot\hat{n}\,dS = 4\pi\int\tilde{\rho}\,dV + 4\pi\int\sigma\,dS, \tag{2.16}$$

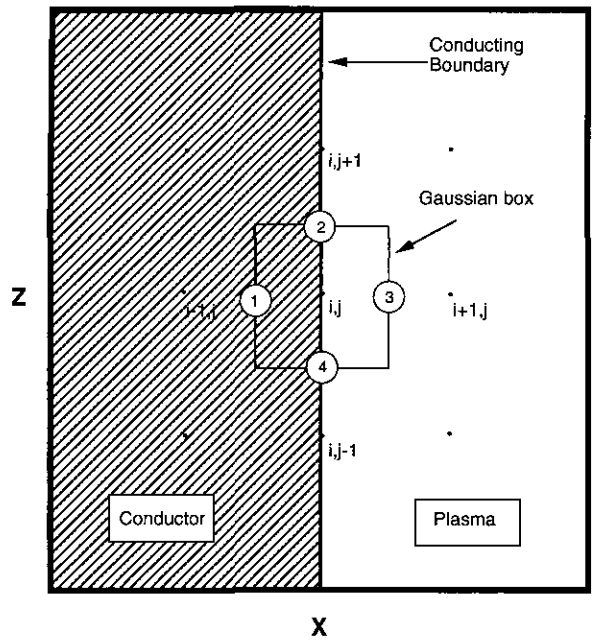

FIG. 1. Position of the surfaces for a Gaussian box around a node at the surface of a conducting boundary.

where σ is the surface charge density on the conductor. Consider a conducting wall with surface normal in the positive x direction and a boundary node at i, j with a Gaussian box around it located at half grid points as in Fig. 1. The integral on the left-hand side of Eq. (2.16) can be split over the four surfaces. Assuming the variables are constant over a surface and are equal to the value of the variables at the center of the surface, the integrals are easily evaluated:

$$\int_1 (\mathbf{I} + 4\pi\mathbf{X})\mathbf{E}\cdot(-\hat{x})\,dy\,dz = 0$$

$$\int_2 (\mathbf{I} + 4\pi\mathbf{X})\mathbf{E}\cdot(\hat{z})\,dx\,dy = [4\pi X^{31}E^x + (1 + 4\pi X^{33})E^z]_{i,j+1/2}\,\Delta x\,\Delta_y$$

$$\int_3 (\mathbf{I} + 4\pi\mathbf{X})\mathbf{E}\cdot(\hat{x})\,dy\,dz = [(1 + 4\pi X^{11})E^x + 4\pi X^{13}E^z]_{i+1/2,j}\,\Delta y\,\Delta_z \qquad (2.17)$$

$$\int_4 (\mathbf{I} + 4\pi\mathbf{X})\mathbf{E}\cdot(-\hat{z})\,dx\,dy = -[4\pi X^{31}Ex + (1 + 4\pi X^{33})E^z]_{i,j-1/2}\,\Delta x\,\Delta_y.$$

Inside the conducting wall the field is zero so the integral over surface one is zero. Fields tangent to the equipotential surface are also zero. Finally at the surface $E^n_{i,j} = 4\pi\sigma$ so

$$4\pi \int \sigma\,dS = E^n_{i,j}\,\Delta y\,\Delta z. \qquad (2.18)$$

Putting all this into Eq. (2.16) we find

$$E^x_{i,j} = \frac{2\pi\rho_{i,j}\,\Delta x + [(1 + 4\pi X^{11}_{i+1/2,j})E^x_{i+1/2,j} + 4\pi X^{13}_{i+1/2,j}E^z_{i+1/2,j}]\,\Delta z}{[\Delta z + 4\pi\,\Delta x(X^{31}_{i,j-1/2} - X^{31}_{i,j+1/2})]}. \qquad (2.19)$$

Similar expressions are found for walls with surface normals $-\hat{x}$, $\hat{z}$, and $-\hat{z}$.

When a sheath is not resolved and $\omega_{pe}\Delta t$ is large, Eq. (2.19) is dominated by X^{11}. This results in a large, nonphysical electric field at the conducting surface. Since a sheath is not resolved, the field at the boundary fluctuates due to the simulation particle noise. This is the same as the fluctuating electrostatic fields in the bulk of the plasma, but the anamolously large magnitude of the boundary field causes excessive numerical heating of the plasma. To get realistic fields a sheath boundary condition must be applied which imposes the normal E-field. The field must be set according to the potential drop calculated from an analytic sheath model. We are in the process of implementing such a sheath boundary condition for the code. The results presented in this paper use a relatively simple sheath model. The ions are represented as a uniform, stationary positive background. The potential drop of the sheath is represented by a boundary condition on the particles as well as the field. An infinite potential drop in the sheath is implemented by specularly reflecting all of the particles at conducting walls. Since the potential drop is already represented by particle reflection the E-field is set to zero at the walls. The result is that the particles remain in the simulation region instead of being absorbed, and they are not heated due to anomalously large fluctuating fields at the walls.

3. *Numerical Solution of the Field Equation*

Given the nine-point stencil for the difference equation and the large, sparse, nondiagonally dominant matrix, the bi-conjugate gradient (BCG) method was chosen to solve the implicit electrostatic equation. The BCG method is a variation of the conjugate gradient method applicable to nonsymmetric matrices. The conjugate gradient method is an iterative minimization of the functional $\phi(x) = 0.5x^{\mathrm{T}}Ax - x^{\mathrm{T}}b$ [20]. At the minimum $\nabla\phi = Ax - b = 0$ so we have solved the matrix equation $Ax = b$. In the BCG method two residual and two conjugate vectors are defined [21]. The method is not guaranteed to converge. For those cases where it does converge, the method is guaranteed to converge in n iteractions for an n-dimensional space. In practice a useful solution can usually be obtained in far fewer than n iterations.

Conjugate gradient schemes converge more rapidly for well-conditioned matrices. Preconditioning transforms $Ax = b$ into a well-conditioned system through an incomplete LU decomposition of the matrix A. The sparsity pattern of A is used in determining which terms in L and U are calculated thus minimizing the computations required to perform the decomposition. From Anderson *et al.* [22] the preconditioned system is $Mu = C$, where $M = L^{-1}AU^{-1}$, $u = Ux$, and $C = L^{-1}b$. We

use the optimized preconditioned bi-conjugate gradient routine CPDES 2 [22] for nonperiodic and periodic simulations, and our own version for doubly periodic problems. We have not had problems with convergence in our simulations.

B. Darwin Method

1. *Field Equations*

The Darwin limit of Maxwell's equations is obtained by dropping the solenoidal part of the displacement current [6] to obtain

$$\begin{aligned} \nabla \cdot \mathbf{E}_{\text{irr}} &= 4\pi\rho, \quad \nabla \times \mathbf{E} = -\frac{1}{c}\frac{\partial \mathbf{B}}{\partial t} \\ \nabla \cdot \mathbf{B} &= 0, \qquad \nabla \times \mathbf{B} = \frac{4\pi}{c}\mathbf{J} + \frac{1}{c}\frac{\partial \mathbf{E}_{\text{irr}}}{\partial t}. \end{aligned} \tag{2.20}$$

Using the charge continuity equation, we can replace $\dot{\mathbf{E}}_{\text{irr}}$ with $-4\pi\mathbf{J}_{\text{irr}}$ and rewrite Ampere's law as

$$\nabla \times \mathbf{B} = \frac{4\pi}{c}\mathbf{J}_{\text{sol}}. \tag{2.21}$$

Consider $\mathbf{E}$ and $\mathbf{B}$ in terms of the potentials ϕ and $\mathbf{A}$ in the Coulomb gauge ($\nabla \cdot \mathbf{A} = 0$):

$$\begin{aligned} \mathbf{B} &= \nabla \times \mathbf{A} \\ \mathbf{E} &= -\nabla\phi - \frac{1}{c}\frac{\partial \mathbf{A}}{\partial t}. \end{aligned} \tag{2.22}$$

Using these potentials in the Darwin field equations, we find the following equations for the fields. For the electrostatic potential we find the usual Poisson's equation

$$\nabla^2\phi = -4\pi\rho. \tag{2.23}$$

This equation was modified in Section II.A to allow an implicit particle advance with respect to the electrostatic field. As shown below, the time advanced $\mathbf{E}_{\text{irr}}$ can then be used along with the time advanced particle quantities to construct a source term for the $\mathbf{E}_{\text{sol}}$ equation. In a 2D code we use two forms to solve for the B-field in order to ensure that $\nabla \cdot \mathbf{B} = 0$ and $\nabla \cdot \mathbf{A} = 0$. For the component of $\mathbf{B}$ which is out of the simulation plane, the y component, we can take the curl of Ampere's law which gives

$$\nabla^2 B_y = -\frac{4\pi}{c}(\nabla \times J)_y. \tag{2.24}$$

Since there is no variation of quantities in the y direction, this component of $\mathbf{B}$ cannot contribute to the divergence of $\mathbf{B}$. The second equation is obtained by replacing $\mathbf{B}$ in Ampere's law with its vector potential form. This gives

$$\nabla^2 A_y = -\frac{4\pi}{c} J_{\text{sol},y}. \tag{2.25}$$

Again with no variation in y, A_y and J_y are automatically solenoidal. Finally combining the two curl equations we find

$$\nabla^2 \mathbf{E}_{\text{sol}} = \frac{4\pi}{c^2}\dot{\mathbf{J}}_{\text{sol}}. \tag{2.26}$$

Now we can utilize the first velocity moment of the Boltzmann equation, sum over species, and find $\dot{\mathbf{J}}$ in terms of present particle quantities,

$$\begin{aligned} \frac{4\pi}{c^2}\dot{\mathbf{J}} &= \mu\mathbf{E}_{\text{sol}} + \mu\mathbf{E}_{\text{irr}} + \zeta \times \mathbf{B} + \mathbf{K} \\ &= \mu\mathbf{E}_{\text{sol}} + \mathbf{Q}, \end{aligned} \tag{2.27}$$

where

$$\begin{aligned} \mu &= \sum_s \frac{\omega_{ps}^2}{c^2} \\ \zeta &= \frac{4\pi}{c^3}\sum_s \frac{q_s}{m_s}\mathbf{J}_s \\ \mathbf{K} &= -\frac{4\pi}{c^2}\sum_s q_s \nabla \cdot \langle \mathbf{vv} \rangle_s. \end{aligned} \tag{2.28}$$

Putting Eq. (2.27) in terms of a direct accumulation of the particle quantities [23] produces

$$\begin{aligned} \dot{\mathbf{J}}_s(\mathbf{x}_j) = &-q_s \sum_i \mathbf{v}_i \mathbf{v}_i \cdot \nabla_j S(\mathbf{x}_j - \mathbf{x}_i) \\ &+ \left(\frac{q_s^2}{m_s}\right) \sum_i S(\mathbf{x}_j - \mathbf{x}_i) \left[\mathbf{E}(\mathbf{x}_i) + \frac{\mathbf{v}_i \times \mathbf{B}(\mathbf{x}_i)}{c}\right]. \end{aligned} \tag{2.29}$$

This solution is implemented since the use of a finite difference of $\dot{\mathbf{B}}$ or $\dot{\mathbf{J}}$ leads to a problem size limit of less than $2\pi c/\omega_p$ in order to prevent instability [6]. We now have a set of elliptic equations that generates instantaneous fields given the time advanced particle source terms.

The effect of the Darwin approximation is evident in the change of the solution to the vector potential form of Ampere's law. The fully electrodynamic form is

$$\nabla^2 \mathbf{A} - \frac{1}{c^2}\frac{\partial^2 \mathbf{A}}{\partial t^2} = -\frac{4\pi}{c}\mathbf{J}_{\text{sol}} \tag{2.30}$$

with the solution

$$\mathbf{A}(\mathbf{x}, t) = \int \frac{\mathbf{J}_{\text{sol}}(\mathbf{x}', t - |\mathbf{x} - \mathbf{x}'|/c)}{|\mathbf{x} - \mathbf{x}'|} d^3x'. \tag{2.31}$$

If the partial derivative with respect to time is dropped in Eq. (2.30), the solution becomes

$$\mathbf{A}(\mathbf{x}, t) = \int \frac{\mathbf{J}_{\text{sol}}(\mathbf{x}', t)}{|\mathbf{x} - \mathbf{x}'|} d^3x'. \tag{2.32}$$

It is obvious that retardation effects due to the finite propagation time of light have been eliminated. In a vacuum light waves no longer exist.

Linear theory provides the dispersion characteristics of the Darwin limit in plasma. As expected longitudinal waves, such as plasma oscillations, are unaffected. However, the absence of the solenoidal part of the displacement current does have major consequences for transverse waves. Fast waves (those with phase velocities larger than c) are nonpropagating. For example, in a Darwin plasma with no imposed fields the dispersion relation for transverse waves is $-c^2k^2 = \omega_{pe}^2(1 + Zm_e/m_i)$. This results in imaginary k or spacially damped fields. The magnitude of the effect on slow waves depends on the plasma characteristics. As discussed by Kaufman and Rostler [24], in a magnetized plasma $(ck/\omega)^2_{\text{Darwin}} \sim (ck/\omega)^2_{\text{Maxwell}} - 1$. So Darwin is best used for those phenomena where transverse wave velocities as well as particle velocities are significantly less than the speed of light.

2. *Streamlined Darwin Field (SDF) Formulation*

Equation (2.26) presents some difficulties in finding its solution. A computationally intensive vector decomposition of $\dot{\mathbf{J}}$ is required to find its solenoidal part, and this can only be done if we can specify boundary conditions for the decomposition. In many applications boundary conditions on the irrotational part of $\dot{\mathbf{J}}$ cannot be determined. Early applications generally considered problems where boundaries were distant from the plasma. A uniform plasma with doubly periodic boundaries is an example of this kind of simulation. Even in this case a slow iterative process must be used to solve Eq. (2.26) since $\mathbf{E}_{\text{sol}}$ appears on the right-hand side of the equation. First an expression for $\dot{\mathbf{J}}$ must be generated, decomposed, and used as the right-hand side for Eq. (2.26). After solving Eq. (2.26) for $\mathbf{E}_{\text{sol}}$, the process is repeated until convergence.

Hewett and Boyd derived the streamlined Darwin field (SDF) formulation to avoid both boundary condition and vector decomposition problems [2]. They defined new field quantities as

$$-\nabla^2(\nabla\psi) \equiv \frac{4\pi}{c^2}\dot{\mathbf{J}}_{\text{irr}} \tag{2.33}$$

$$\boldsymbol{\Xi} \equiv \mathbf{E}_{\text{sol}} - \nabla\psi. \tag{2.34}$$

Recalling the form of the $\mathbf{E}_{\text{sol}}$ field equation

$$\nabla^2\mathbf{E}_{\text{sol}} = \mathbf{Q} + \mu\boldsymbol{E}_{\text{sol}} - \frac{4\pi}{c^2}\dot{\mathbf{J}}_{\text{irr}}, \tag{2.35}$$

we find two coupled partial differential equations in terms of $\boldsymbol{\Xi}$ and ψ,

$$\nabla^2\boldsymbol{\Xi} - \mu\,\boldsymbol{\Xi} = \mathbf{Q} + \mu\nabla\psi \tag{2.36}$$

$$\nabla^2\psi = -\nabla\cdot\boldsymbol{\Xi}. \tag{2.37}$$

Many of the previous problems in solving $\boldsymbol{E}_{\text{sol}}$ have now been eliminated. A vector decomposition of $\mathbf{Q}$ is no longer required so nonintuitive boundary conditions do not have to be determined. Equation (2.37) ensures that the solution for $\boldsymbol{E}_{\text{sol}}$ is in fact solenoidal. As we shall see in the next section, boundary conditions on $\boldsymbol{\Xi}$ and ψ are straightforward and depend on the boundary conditions on $\boldsymbol{E}_{\text{sol}}$.

3. *Boundary Conditions on A_y, B_y, and $\mathbf{E}_{\text{sol}}$*

As with the electrostatic potential, the SDF field solvers in the code allow periodic, Dirichlet, and Neumann boundary conditions for A_y, B_y, and $\mathbf{E}_{\text{sol}}$. While periodic and symmetric boundaries require the same conditions for all fields as described in Section II.A, conducting surfaces impose conditions which must be applied separately for the different field components. Since the B-field has no divergence and is zero inside a perfect conductor, the normal component of the field is zero on the surface of the conductor. To meet this condition A_y must be a constant along the surface of a conductor. Thus we have a Dirichlet zero boundary condition on A_y.

Considering $\mathbf{E}$ on a perfectly conducting surface, we find from Ampere's law and Gauss' law that $E_t = 0$ and $E_n = 4\pi\sigma$ on the surface, where t is for tangential and n is for normal. From $E_t^{\text{sol}} = 0$ along the boundary we find $\partial_t E_t^{\text{sol}} = 0$. Since $\nabla\cdot\mathbf{E}_{\text{sol}} = 0$, this implies $\partial_n E_n^{\text{sol}} = 0$. Given that $\mathbf{E}_{\text{sol}} = 0$ inside the conductor, we have $E_n^{\text{sol}} = 0$ on the surface. The surface charge must be accounted for by E_{irr} so $E_n^{\text{irr}} = 4\pi\sigma$. Thus we continue to satisfy Gauss' law with $-\nabla\phi$. This leaves us with $\mathbf{E}_{\text{sol}} = 0$ on conductors.

We want boundary conditions on $\boldsymbol{\Xi}$ and ψ which will enforce the above condition while still maintaining $\nabla\cdot\mathbf{E}_{\text{sol}} = 0$. This is done with the following set of equations:

(1) For nonboundary and Neumann points, solve the SDF equations (2.36) and (2.37). For Neumann zero points, require $\partial_n\psi = 0$ and $\partial_n\boldsymbol{\Xi} = 0$.

(2) For conductor interiors set

$$\boldsymbol{\Xi} = -\nabla\psi, \quad \psi = 0. \tag{2.38}$$

We have a simple Dirichlet boundary condition on ψ while maintaining $\mathbf{E}_{\text{sol}} = 0$. The divergence of $\mathbf{E}_{\text{sol}}$ remains zero since $\mathbf{E}_{\text{sol}}$ is constant everywhere inside the conductor.

(3) For conductor surfaces set

$$\boldsymbol{\Xi} = -\nabla\psi, \quad \nabla^2\psi = -\nabla\cdot\boldsymbol{\Xi}. \tag{2.39}$$

This ensures that $\Xi + \nabla\psi$ is solenoidal at the surface of the conductor. Since $\Xi = -\nabla\psi$ applies only inside and on the surface of the conductor, the derivative of the equation may be discontinuous as the interface is crossed. So the divergence cleaning relation must be explicitly enforced on the surface.

(4) Driven conductors can be treated in two ways. The first option is as Dirichlet points, where $\mathbf{E}_{sol}$ is specified. The second is as nonboundary points where the driven current density $\mathbf{J}_d^{sol}$ is added to the appropriate component of $\mathbf{Q}$ in each of the nodes inclusive to the conductor. Since this is an imposed current density not dependent upon what occurs in the simulation, we simply define this current density to be whatever we want. Since we may choose not to resolve the skin depth of the conductor with our grid, the current density is set to get the correct total current given the size of the conductor. This still leads to reasonably correct fields outside the conductor.

4. *Numerical Solution of the SDF Equations*

Dynamic alternating direction implicit (DADI) is the method used to find solutions to the system of finite difference equations resulting from SDF. DADI is an iterative, operator-splitting technique where a fictitious time step is added to the equation to be solved,

$$-\frac{\partial\psi}{\partial t} = L\psi, \tag{2.40}$$

where L is the operator resulting from the finite difference form of the original equations. For a discussion of the basic technique see [25]. Iterating Eq. (2.40) to the time-asymptotic state, we find a solution to $L\psi = 0$. The idea is to split the operator into pieces which can be easily solved implicitly and to take several steps to advance ψ from fictitious time step n to $n + 1$. The splitting can be chosen to ensure convergence of the method [7]. For this case consider a single splitting into the horizontal, H, and vertical, V, parts of the Laplacian operator,

$$\begin{aligned}(-\omega + H)\psi^{n+1/2} &= (-\omega - V)\psi^n + \sigma\\ (-\omega + V)\psi^{n+1} &= (-\omega - H)\psi^{n+1/2} + \sigma,\end{aligned} \tag{2.41}$$

where

$$\begin{aligned}H\psi &= (\psi_{i+1,j} - 2\psi_{i,j} + \psi_{i-1,j})/\Delta x^2\\ V\phi &= (\psi_{i,j+1} - 2\psi_{i,j} + \psi_{i,j-1})/\Delta z^2.\end{aligned} \tag{2.42}$$

Given the form of the operator a simple tridiagonal solve is all that is necessary for each H or V pass. The subtlety comes in choosing the size of each time step to maximize the rate at which we approach the time asymptotic state or, equivalently, the rate of convergence. The method used here is due to Doss and Miller as applied to the Laplacian operator [26]. This method is used for the B-field and vector potential, Eqs. (2.24) and (2.25), respectively.

For the SDF equations coupled equation DADI (CEDADI) as discussed by Hewett, Larson, and Doss [7] is used. The horizontal and vertical passes in this case become

$$\begin{aligned}&\text{H} - \text{PASS}\\ (-\omega + H - f\mu)\Xi_x^{n+1/2} &= (-\omega - V + (1-f)\mu)\Xi_x^n\\ &\quad + \mu D_x\psi^n + Q_x\\ (-\omega + H - f\mu)\Xi_y^{n+1/2} &= (-\omega - V + (1-f)\mu)\Xi_y^n + Q_y\\ (-\omega + H - f\mu)\Xi_z^{n+1/2} &= (-\omega - V + (1-f)\mu)\Xi_z^n\\ &\quad + \mu D_z\psi^n + Q_z\\ (-\omega + H)\psi^{n+1/2} &= (-\omega - V)\psi^n - D_x\Xi_x^n - D_z\Xi_z^n\\ &\text{V} - \text{PASS}\\ (-\omega + V - f\mu)\Xi_x^{n+1} &= (-\omega - H + (1-f)\mu)\Xi_x^{n+1/2}\\ &\quad + \mu D_x\psi^n + Q_x\\ (-\omega + V - f\mu)\Xi_y^{n+1} &= (-\omega - H + (1-f)\mu)\Xi_y^{n+1/2} + Q_y\\ (-\omega + V - f\mu)\Xi_z^{n+1} &= (-\omega - H + (1-f)\mu)\Xi_z^{n+1/2}\\ &\quad + \mu D_z\psi^n + Q_z\\ (-\omega + V)\psi^{n+1} &= (-\omega - H)\psi^{n+1/2} - D_x\Xi_x^n - D_z\Xi_z^n,\end{aligned} \tag{2.43}$$

where

$$\begin{aligned}D_x\psi_{i,j} &= (\psi_{i+1,j} - \psi_{i-1,j})/(2\Delta x)\\ D_z\psi_{i,j} &= (\psi_{i,j+1} - \psi_{i,j-1})/(2\Delta z)\\ 0 \le f &\le 1.\end{aligned} \tag{2.44}$$

Note that all of the first-order derivative terms are lagged (evaluated with nth-iteration values). This has been found to be necessary to keep the algorithm stable [7]. This also allows the continued use of a tridiagonal solve for the implicit terms. The CEDADI method has been shown to be considerably faster than biconjugate gradient for this set of equations.

C. Dielectrics

For many problems of interest we need dielectric as well as conducting structures. Since fields penetrate through dielectrics, we cannot simply treat them as surfaces with boundary conditions which ignore the interior. For dielectrics Ampere's law in the Darwin limit becomes

$$\nabla \times \mathbf{B} = \frac{4\pi}{c}\mathbf{J} + \frac{1}{c}\frac{\partial \mathbf{D}_{int}}{\partial t}. \tag{2.45}$$

Here $\mathbf{D}$ is the electric displacement which we define as

$$\mathbf{D} = (1 + 4\pi X_d)\mathbf{E}, \tag{2.46}$$

where X_d is the dielectric susceptibility. Note that in the plasma where X_d is zero, we have the same equations as the previous section. So the accuracy for the particle Lagrangian remains the same.

In the dielectric region we use Gauss' law

$$\nabla \cdot \mathbf{D} = 4\pi\rho \tag{2.47}$$

and the charge continuity equation to replace $\mathbf{D}_{\text{irr}}$ with $-4\pi\mathbf{J}_{\text{irr}}$. Again we can write Ampere's law as Eq. (2.21). The result is that the equations for $\mathbf{E}_{\text{sol}}$ and $\mathbf{B}$ are unchanged. All the solutions of the previous section still apply. This is not the case for the electrostatic field equation where Gauss' law in terms of the components of the E-field becomes

$$\nabla \cdot [(1 + 4\pi X_d)\nabla\phi] - \nabla \cdot (4\pi X_d \mathbf{E}_{\text{sol}}) = -4\pi\rho. \tag{2.48}$$

Solving for the electrostatic potential including the direct implicit susceptibility, $\mathbf{X}_I$, we find a new electrostatic field equation

$$\nabla \cdot [(\mathbf{I} \cdot + 4\pi\mathbf{X}_I \cdot + 4\pi X_d)\nabla\phi^{n+1}] = -4\pi\tilde{\rho} + 4\pi\mathbf{E}^n_{\text{sol}} \cdot \nabla X_d. \tag{2.49}$$

This equation introduces a possible stability problem since the electrostatic and electromagnetic field equations allow an explicit connection between $\mathbf{E}^n_{\text{sol}}$ and $\mathbf{E}^{n+1}_{\text{sol}}$ during a time step. This should only be a problem in regions where dense plasma and dielectric meet. In the plasma X_d is zero so the connection through the electrostatic equation is removed. In regions of dielectric and vacuum the $\mu\mathbf{E}_{\text{irr}}$ term is absent from $\mathbf{Q}$ as defined by Eq. (2.27). It does not contribute to the SDF equation (2.36); therefore, there is no contribution to $\mathbf{E}_{\text{sol}}$. Since we anticipate treating plasma/wall interfaces with analytic sheath boundary conditions, the potential region of instability will be eliminated from the simulation. As a second option for those cases where $\mathbf{E}_{\text{sol}}$ makes little contribution to Eq. (2.49), the $\mathbf{E}^n_{\text{sol}} \cdot \nabla X_d$ term could be removed while retaining most of the contribution of X_d. This is true for situations in which $\mathbf{E}_{\text{sol}}$ is driven in the direction perpendicular to the simulation plane, and the only contributions to $\mathbf{E}_{\text{sol}}$ in the plane are plasma fluctuations.

D. Combined Algorithm and GYMNOS

We can now integrate the field solves of Section II.A and II.B into a combined algorithm for the time advance of particle and field quantities. The result is a time cycle of two sets of the four steps mentioned in Section I. Given initial values of $\mathbf{E}^n$, $\mathbf{B}^n$, $\mathbf{x}^n_i$, $\mathbf{v}^{n-1/2}_i$, and $\bar{\mathbf{a}}^{n-1}_i$, we proceed as follows:

I. Advance to $\sim$ level

(1) Interpolate $\mathbf{E}^n_{\text{sol},j}$ and $\mathbf{B}^n_j$ to particles.

(2) Push particles to $\tilde{\mathbf{v}}_i$ and $\tilde{\mathbf{x}}_i$ using Eq. (2.6).

(3) Interpolate the $\tilde{\mathbf{v}}_i$ and $\tilde{\mathbf{x}}_i$ to the grid to get $\tilde{\rho}_j$ and $\mathbf{X}_j$.

(4) Solve the implicit electrostatic field equation (2.49) to find $\mathbf{E}^{n+1}_{\text{irr},j}$

II. Advance to $n+1$ level

(1a) Interpolate $\mathbf{E}^{n+1}_{\text{irr},j}$ and $\mathbf{B}^n_j$ to particles

(2a) Push particles to $\mathbf{v}^{n+1/2}_i$ and $\mathbf{x}^{n+1}_i$ using Eq. (2.7) and evaluating δv at $\tilde{\mathbf{x}}$. Save $\bar{\mathbf{a}}^n$.

(1b) Interpolate $\mathbf{E}^{n+1}_{\text{irr},j}$, $\mathbf{E}^n_{\text{sol},j}$, and $\mathbf{B}^n_j$ to particles

(2b) Find $\mathbf{v}^{n+1}_i$ from

$$\mathbf{v}^{n+1} = \mathbf{R}^n \cdot \mathbf{v}^{n+1/2} + \frac{q\Delta t}{4m}(\mathbf{I} + \mathbf{R}^n) \cdot (\mathbf{E}^{n+1}_{\text{irr}} + \mathbf{E}^n_{\text{sol}}) \tag{2.50}$$

(3) Interpolate the $\mathbf{v}^{n+1}_i$ and $\mathbf{x}^{n+1}_i$ to the grid to get $\mathbf{J}^{n+1}_j$, ρ^{n+1}_j, and $\mathbf{K}^{n+1}_j$.

(4) Solve the B-field and SDF equations (2.24), (2.25), (2.36), and (2.37) to find $\mathbf{B}^{n+1}_j$ and $\mathbf{E}^{n+1}_{\text{sol},j}$.

Since the solution of the electrostatic and SDF fields are separated in this algorithm, there is certainly flexibility with respect to the method used for the implicit electrostatic particle advance. We have chosen the D1 direct implicit scheme, but other direct implicit schemes or the moment implicit method could be substituted with little change to the overall algorithm.

Note that steps (1), (2), and (3) are inside a loop over all the particles. The steps are completed for one particle before the next particle is considered. Each particle adds its contribution individually to the grid source terms in step (3). Also $\mathbf{v}^{n+1}$ is not stored for each particle. The advance of one-half a time step is needed to find $\mathbf{J}^{n+1}$ and $\mathbf{K}^{n+1}$. Only the second-order accurate, leap-frogged $\mathbf{v}^{n+1/2}$ passes through to the next time cycle.

This algorithm has been incorporated into an already existing 2.5D PIC code developed by Hewett called GYMNOS [27]. This magnetostatic code based on elliptic solving algorithms using DADI is an excellent framework for the DADIPIC algorithm. The code is written in R-Z geometry and has the ability to generate its own internal structures. Both structure and field quantities are stored on cell corners. Particles may be perfectly reflected, fully absorbed, absorbed with a fraction thermally reemitted, field-emitted, or injected with a prescribed distribution. The particle pusher is a fully vectorized Boris pusher. The status of nodes in relation to structures is stored in geometry arrays. These arrays are needed in the field solve and particle trapping routines since the handling of nodes in the routines is controlled with integer switches.

For the implementation of DADIPIC, GYMNOS was converted to XZ geometry. This allowed the investigation of DADIPIC in a uniform doubly periodic plasma where comparisons could be made to analytic kinetic theory for basic test cases. The two parts of the time cycle in DADIPIC manifest themselves in the duplication of the routines called during a time step.

The number of geometry arrays has been increased to allow different structure types. All nodes in structures are boundary nodes for the particles. Dielectric structures do not generate boundary nodes for fields. The grid nodes do have an associated dielectric susceptibility which is set according to the locations of the dielectric structures. Before each field solution, node designators are set with any driven structures removed. As an example consider a conducting structure which has a driven current density in the y direction. For the electrostatic field solve the structure would have Dirichlet nodes at some designated potential. For the A_y solve the structure is not a boundary region, and the structure nodes have some imposed current density added to any particle density at each point.

III. TEST CASES

In this section we present two test cases to demonstrate the ability of DADIPIC to simulate electromagnetic phenomena under conditions of large $\omega_{pe}\Delta t$ and $\Delta x/\lambda_{De}$.

A. Uniform Plasma: Electron Cyclotron Waves

We investigated electron cyclotron waves to test the algorithm's ability to simulate low frequency oscillations without the complications of boundary conditions. These right circularly polarized waves propagate along the B-field lines in a magnetized plasma. The dominant interaction is between the particles and the electromagnetic (Darwin) fields. The electrostatic field maintains charge neutrality in the fluctuating but essentially uniform plasma. Without large density gradients or nonneutral regions the direct implicit method only serves the function of allowing us to use large time steps while retaining electron kinetics. The B-field is chosen so $\omega_{ce} \ll \omega_{pe}$, where ω_{ce} is taken as a positive quantity. This gives a phase velocity much less than c, making the Darwin approximation reasonable. The cold plasma dispersion relation is [28]

$$\frac{c^2k^2}{\omega^2} = 1 + \frac{\omega_{pe}^2}{(\omega_{ce} - \omega)\omega}. \tag{3.1}$$

In the simulations $\omega_{ce}/\omega_{pe} = 0.01$, the density is 10^8 cm^{-3}, and the number of particles per cell is 30. The simulation region is periodic in both the x and z directions, and the imposed B-field, B_o, is applied in the z direction. The spacial and temporal discretization is set so that $\omega_{pe}\Delta t = 20$ and $\Delta x/\lambda_{De} = 70$ or $\omega_{pe}\Delta t = 40$ and $\Delta x/\lambda_{De} = 140$. These parameters are chosen to satisfy the constraints of resolving the wavelengths, resolving the frequency, and residing near the energy conserving contour, $3v_{th}\Delta t/\Delta x \sim 1$ [16]. The plasma thermal velocities needed to achieve these constraints are not large enough to make any observable change in the oscillation frequency from the cold plasma dispersion relation.

Several simulations both with and without initial perturbations were run. In the first type a wave is initialized in the plasma with the size of the simulation region in the z direction set to one wavelength. The grid is 64 nodes in z and 8 in x. Two spacial dimensions are not necessary here, but this does verify the operation of the 2D field solvers. The relationships between the perturbed fluid velocities and perturbed fields derived from linear theory are

$$\begin{aligned}
\mathbf{B}_1 &= v_1 B_o \frac{k(\omega - \omega_{ce})}{\omega\omega_{ce}} [-\hat{x}\sin(kz) - \hat{y}\cos(kz)] \\
\mathbf{E}_1 &= v_1 B_o \frac{(\omega - \omega_{ce})}{c\omega_{ce}} [-\hat{x}\cos(kz) - \hat{y}\sin(kz)] \\
\mathbf{v}_1 &= v_1[\hat{x}\sin(kz) + \hat{y}\cos(kz)].
\end{aligned} \tag{3.2}$$

The particles are loaded according to a drifted maxwellian with the drift velocity having the functional form of Eq. (3.2). To ensure resolution of v_1 given the set ratio of Δt and Δx, v_1 is set to $0.25v_{the}$. The resulting perturbed B-fields are less than 5% of B_o.

The resulting fields verified that the right-hand sides of the $\mathbf{B}$ and $\mathbf{E}_{sol}$ equations were derived correctly and that the field solving routines were calculating the expected solutions. This also allowed us to determine if particle noise in terms such as the kinetic energy tensor, $\mathbf{K}$, might cause excessive noise in the resulting fields. Given the magnitude of v_1, the fluctuations in $\mathbf{v}$ are not much smaller than the imposed perturbation. As shown in Fig. 2, the initial fields agree with Eq. (3.2). The initialized parameters are $v_1 = 1.025 \times 10^7$ cm/s and $ck/\omega_{pe} = 1$ which should give field magnitudes of $|\mathbf{E}_1|/B_o = 1.7 \times 10^{-4}$ and $|\mathbf{B}_1|/B_o = 0.034$. Energy conservation for this whole group of simulations ranged from 1% to 3% due to electrostatic fluctuations. The frequency of oscillation was recorded for several different initial wavelengths to compare to the analytic dispersion curve for the real part of the frequency.

The second type of simulation is a uniform, unperturbed plasma where peaks in the electromagnetic spectral density indicate the dispersion relation for electron cyclotron waves. The fourier transform in space and time is recorded for $B_x^2(k_x, \omega)$. A square 32×32 grid is used in this case. The results of both types of simulations agree with the analytic dispersion relation as indicated by Fig. 3.

In the warm plasma the particles see the Doppler shifted frequency of the wave, $\omega' = \omega - v_\parallel k$, where $v_\parallel$ is the particle velocity along the B-field. When the force on the particles due to the transverse E-field varies in time near the gyrofrequency of the particles, ω_{ce}, a resonant interation between the wave and the particles occurs, providing a kinetic test for DADIPIC. However, to get the correct damping, the distribution function near $(\omega - \omega_{ce})/kv_{the}$ must be well resolved. Unfortunately, damping which is smaller than the oscillation frequency occurs when the resonance is with particles far out in the tail of the distribution. To overcome this we set up a plasma with two negative species. The first is a dense, cold species which deter-

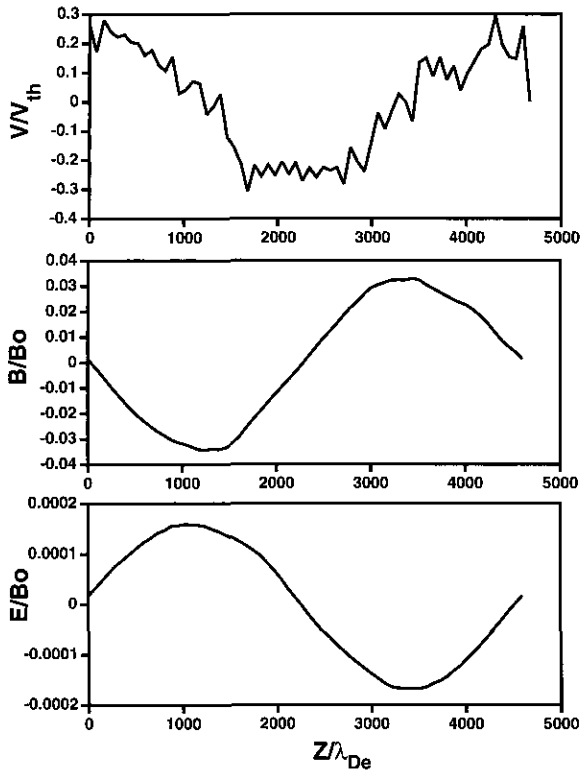

FIG. 2. The grid velocity, v_y, and the generated fields, B_x and $E_{sol,y}$, for an electron cyclotron wave initialized in the particle distribution of a DADIPIC simulation.

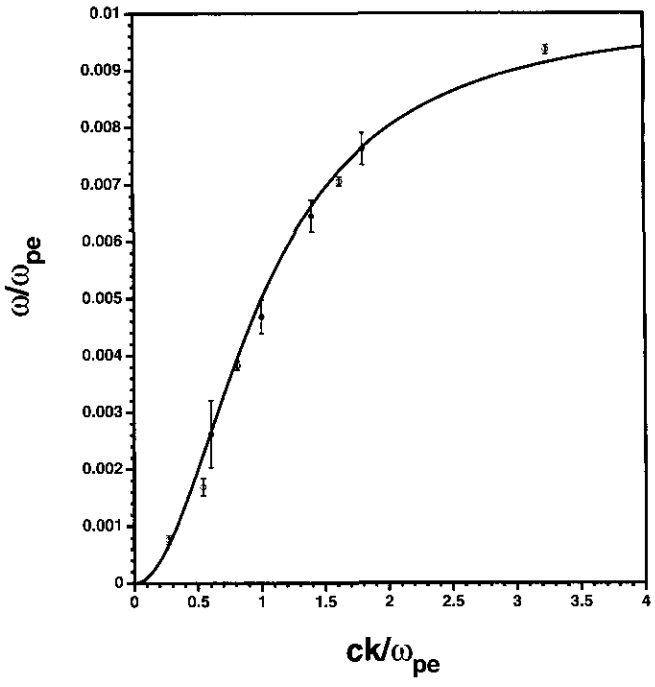

FIG. 3. Electron cyclotron wave dispersion relation for the real part of the frequency. The solid line is the analytic result for the cold magnetoplasma. The points are the DADIPIC results. The error bars are the fwhm of the peaks in the FFTs.

mines the real part of the frequency. The second is a sparse, hot species which determines the damping. The dispersion relation for the warm plasma becomes [29]

$$\omega^2 - c^2k^2 - \frac{\omega_{pe,\mathrm{cold}}^2\omega}{(\omega_{ce,\mathrm{cold}} - \omega)\omega}\left(1 + \frac{k^2v_{the,\mathrm{cold}}^2}{(\omega - \omega_{ce,\mathrm{cold}})^2}\right) - i\sqrt{\frac{\pi}{2}}\frac{\omega_{pe,\mathrm{cold}}\omega}{k\lambda_{De,\mathrm{cold}}}\exp\left[-\frac{(\omega - \omega_{ce,\mathrm{cold}})^2}{2(kv_{the,c})^2}\right] - \frac{\omega_{pe,\mathrm{hot}}^2\omega}{(\omega_{ce,\mathrm{hot}} - \omega)\omega}\left(1 + \frac{k^2v_{the,\mathrm{hot}}^2}{(\omega - \omega_{ce,\mathrm{hot}})^2}\right) - i\sqrt{\frac{\pi}{2}}\frac{\omega_{pe,\mathrm{hot}}\omega}{k\lambda_{De,\mathrm{hot}}}\exp\left[-\frac{(\omega - \omega_{ce,\mathrm{hot}})^2}{2(kv_{the,\mathrm{hot}})^2}\right] = 0. \quad (3.3)$$

The plasma parameters are chosen so only the second, third, and sixth terms contribute. The second species with its low density can be set to cause small damping while its particles are near resonance. In this way there are sufficient PIC particles in the desired region of the distribution. The simulations are 1D so electrostatic fluctuations exist only parallel to the B-field. The cold species has a temperature parallel to the B-field so $\Delta x/\lambda_{De,\mathrm{cold}}$ and $\omega_{pe,\mathrm{cold}}\Delta t$ can be set to prevent heating due to the electrostatic fluctuations. The temperature perpendicular to the B-field is very low so v_1 can dump significantly before being swamped by thermal noise. The plasma parameters are shown in Table II. The damping was varied in several simulations by changing the mass and temperature of the hot species while maintaining $v_{the,\mathrm{hot}}$ constant. This allows us to change the damping and continue to resolve $v_{the,\mathrm{hot}}$.

Figure 4 shows the time histories from a simulation where the hot species mass was two m_e. The B-field recorded at a point (Fig. 4a) is a damped sinusoid as expected. An exponential curve fit to the B-field energy time history (Fig. 4b) provides the estimate to the damping. There is an initial jump in the total system energy (Fig. 4c) of about 1% as the initial load of particles relaxes. Over the rest of the simulation the damping of the electron cyclotron wave and electrostatic fluctuations have little effect on the total system energy. Note that the

TABLE II

Plasma Parameters for Electron Cyclotron Wave Damping

$\omega_{pe,\mathrm{cold}}\,\Delta t = 40$	$\Delta x/\lambda_{De,\mathrm{cold}} = 140$	$n_{\mathrm{grid}} = 64$
$ck/\omega_{pe,\mathrm{cold}} = 0.6$	$v_1/v_{the,\mathrm{cold}} = 0.014$	
$n_0 = 1 \times 10^8\ \mathrm{cm}^{-3}$	$n_{\mathrm{cold}} = 0.98\ n_o$	$n_{\mathrm{hot}} = 0.02\ n_o$
	$T_{\mathrm{cold}} = 0.683$ eV	$T_{\mathrm{hot}} = 4(m_{\mathrm{hot}}/m_{\mathrm{cold}})T_{\mathrm{cold}}$
	$\omega_{ce,\mathrm{cold}} = 0.01\omega_{pe,\mathrm{cold}}$	$\omega_{ce,\mathrm{hot}} = (m_{\mathrm{cold}}/m_{\mathrm{hot}})\omega_{ce,\mathrm{cold}}$

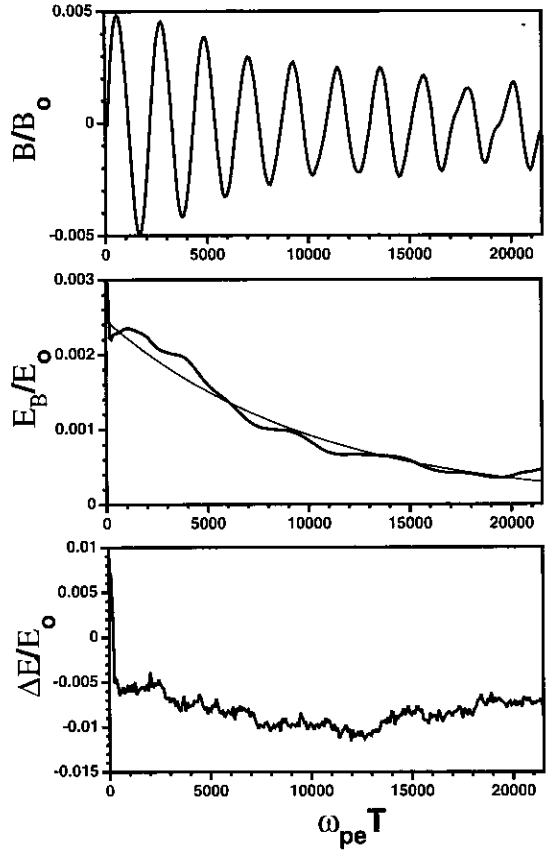

FIG. 4. The time evolution of an electron cyclotron wave simulation (a) the oscillating B-field, (b) the B-field energy with an exponential curve fit, and (c) the change in the total system energy normalized to the initial total system energy.

energy time histories do not include the energy of the applied B-field. The damping observed in several simulations is compared with the damping derived from Eq. (3.3) in Fig. 5. The damping becomes largest near $m_h/m_e = 4$ since the oscillation frequency matches the cyclotron frequency of the hot species. The agreement between DADIPIC and theory is very good over an order of magnitude change in damping rate.

B. Collisionless Heating in Inductively Coupled Plasma Sources

Over the past few years the microelectronics industry has made extensive use of plasmas for etching and deposition on chips. Inductively coupled plasma, ICP, sources have recently been shown to possess promising characteristics [4]. In ICP sources an antenna is current-driven, producing mainly inductive fields. It is separated from the plasma by a dielectric. Electrons accelerated in the inductive fields undergo ionizing collisions with the neutral etching gas in the reactor thus generating and maintaining the plasma. The oscillation of the electrons in the fields coupled with collisions heats the electrons. Heating is one of the processes which determines plasma density, uniformity, and other factors critical for successful etching or deposition. The typical components of a reactor are shown in Fig. 7.

As with any confined plasma, the plasma rises to a positive potential with respect to the walls. This retards the more mobile electrons, allowing the net current to the walls to be zero. Ions, which accelerate across the potential sheath to the chip, may be used for either etching or deposition. A potential different than the wall potential may be applied to the chip, controlling the ion current and ion energy. Unlike capacitive reactors this potential can be completely unrelated to plasma generation. This allows an extra adjustable parameter to achieve the desired ion energy and reduces the capacitive fields in the reactor which might damage the chip. These reactors are typically run at densities around 10^{11} cm^{-3}, a driving frequency of about 10 MHz, neutral pressures of a few mTorr, and electron temperatures of a few eV. The result is an electron-neutral collision frequency, ν, which may be less than the driven frequency, ω. In such cases collisionless heating of the electrons may be as important as resistive heating.

The phenomena of collisionless heating in the ICP is basically the same as that of the anomalous skin effect in metals. Electrons in the conducting medium pass through the skin depth, δ, for EM field penetration and are stocastically heated. Heating is significant for those electrons which reside in the field region

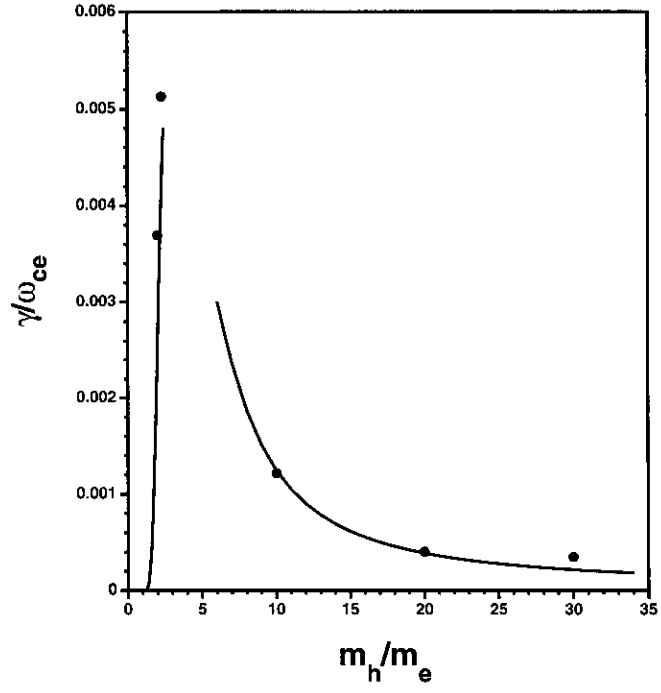

FIG. 5. Electron cyclotron wave damping rate as the hot species mass is changed. The solid line is the analytic damping, and the dots are damping rates measured from DADIPIC simulations. The simulations were all initialized with the same wavelength, $ck/\omega_{pe} = 0.6$.

for a time short compared to the field oscillation period or $\delta/v_{th} \ll \omega^{-1}$. These electrons receive a transverse kick since the inductive E-field remains in one direction over the time of the electron transit of the skin depth. Reuter and Sondheimer derived the 1D kinetic theory for the effect in metals [30] while recently Batchelor *et al.* have made the changes necessary for the plasma case [31]. The theory assumes a harmonic electromagnetic wave normally incident on a half-infinite uniform conducting region. Maxwell's equations, along with the linearized Boltzmann equation for the perturbed electron distribution function, can be solved to find the surface impedance which is proportional to the ratio of the E-field to the B-field. Assuming spacial variation in x and a transverse wave with E_y and B_z, the result at the plasma surface is

$$\frac{E_y}{B_z} = \frac{\sqrt{8}iv_{th}}{\pi c(i + \nu/\omega)} \int_0^\infty dt \Big/ \left(t^2 - \frac{\beta}{(1 - i\nu/\omega)^3} K(t)\right) = \frac{\sqrt{8}iv_{th}}{\pi c(i + \nu/\omega)} I. \tag{3.4}$$

ν is the electron-neutral collision frequency and β is the square of the distance that a thermal electron travels in an rf cycle divided by the collisionless skin-depth or

$$\beta = \frac{4}{\sqrt{\pi}} \left(\frac{v_{th}\omega_{pe}}{\omega c}\right)^2. \tag{3.5}$$

$K(t)$ is a function dependent on the unperturbed electron velocity distribution function. For a Maxwellian plasma we have

$$K(t) = \int_0^\infty dx \frac{2xe^{-x^2}}{t^3} [(1 + (xt)^2) \tan^{-1}(xt) - xt]. \tag{3.6}$$

We can solve Eq. (3.4) numerically for small ν to find E_y/B_z in the collisionless limit. It is more convenient to consider the integral I which depends on the dimensionless parameter β without the proportionality to a particular v_{th}. Figure 6 shows the real and imaginary parts of I versus β. Note that at small β $\mathrm{Re}\{I\} \ll \mathrm{Im}\{I\}$. The effective resistivity is small compared to the inductance, and the electrons simply oscillate in the field without gaining net energy. As β increases the resistive component accounts for a progressively larger proportion of the total surface impedance. From the surface impedance and the magnitude of fields we can find the power deposition in the plasma using the Poynting vector

$$S_x = -\frac{c}{8\pi} \mathrm{Re}\left\{\frac{E_y}{B_z}|B_z|^2\right\} \tag{3.7}$$

where the negative x direction is into the plasma.

A number of 1D simulations compare DADIPIC's ability to

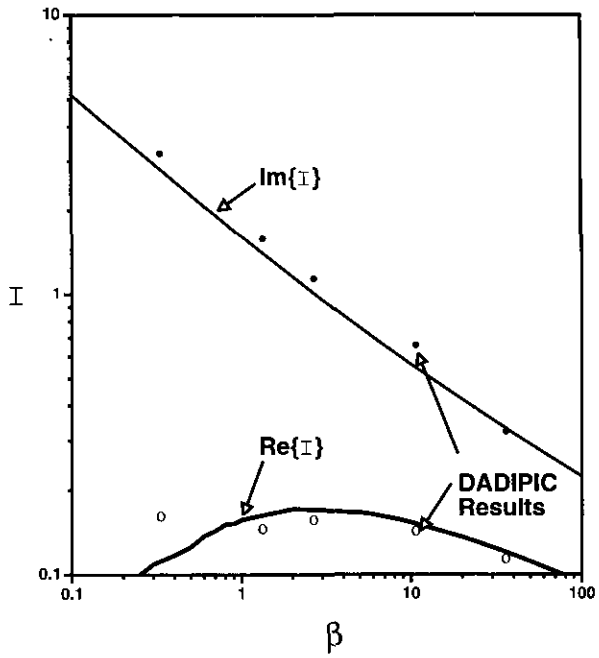

FIG. 6. One-dimensional collisionless heating results in terms of the real and imaginary parts of I vs β in the collisionless limit. At the surface of the plasma $E_y/B_z = 8^{1/2}v_{th}I/\pi c$, and β is the square of the distance traveled by a thermal electron in an rf cycle divided by the collisionless skin depth. The dots are the results of 1D DADIPIC simulations.

reproduce the above analytic results. Our simulations are similar to those of Turner [32]. Conducting walls are placed at the minimum and maximum boundaries in x. Electrons are specularly reflected off of the walls while ions are defined as a stationary neutralizing background. The electron particle number is 16384 and the temperature is 3.75 eV. The total problem length is 14 cm with Δx of 0.14 cm. Δx is chosen to give reasonable resolution of the skin depth which is around 1.5 cm for these simulations. A time-harmonic, solenoidal E-field is imposed on the wall at x maximum. While Turner investigated the relative importance of collisionless heating with respect to collisional heating, our interest is the change of the surface impedance for a collisionless plasma versus β. To vary β between simulations we changed both the plasma density, 10^{11} cm^{-3} to 3×10^{11} cm^{-3}, and the frequency of the imposed E-field, 3.33 MHz to 20 MHz. These densities and frequencies are typical of those in actual plasma processing reactors. The spatial and temporal discretization for the 10^{11} cm^{-3} density is $\Delta x/\lambda_{De} = 31$ and $\omega_{pe}\Delta t = 9$.

Amongst the quantities measured were E_y^{sol} and B_z at the driven wall as well as the change in the total thermal energy of the electrons, ΔE_{th}. With this information we can find the components of I resulting from the simulations with their various β's. The real part is

$$\mathrm{Re}\{I\} = \frac{\pi c}{\sqrt{8}v_{th}} \frac{8\pi(\Delta E_{th}/TA)}{c|B_z|^2}. \tag{3.8}$$

T is the time over which ΔE_{th} is measured and A is the effective surface area of the driven wall, 0.14 cm^2. The magnitudes of E_y^{sol} and B_z, along with Re$\{I\}$, give Im$\{I\}$,

$$\mathrm{Im}\{I\} = \sqrt{\left(\frac{\pi c}{\sqrt{8}v_{th}}\frac{|E_y|}{|B_z|}\right)^2 - \mathrm{Re}\{I\}^2}. \tag{3.9}$$

The results for the simulations appear as dots in Fig. 6. The results for both the imaginary and real parts of I are within 5% to 20% of the analytic solution over an order of magnitude change in β. These results are not in perfect agreement, but the discrepancy appears correctable with finer resolution in the simulations. Calculations with 4096 particles consistently had heating which was low by up to a factor of 2. More particles corrected this problem except for the small β case, $\beta = 0.33$. Here only the particles in the tail of the distribution participate effectively in the heating, and this part of the distribution may still not be sufficiently represented. More particles also decrease the numerical heating/cooling due to fluctuations.

Though the numerical heating is small, <1%, the inductive heating is only about 10% of the total initial particle energy. In order to account for the numerical heating, we measured numerical heating in simulations without driven inductive fields but with all other parameters the same as simulations with driven fields. The amount of numerical heating or cooling was then subtracted or added to the inductive heating results. This is only an approximate correction since the rate of numerical heating changes as the total thermal energy changes. Other improvements to the simulations would be finer resolution of the skin depth and a longer simulation region to better approximate a half infinite plasma. Even though better agreement may be possible, we are encouraged by the accuracy of these simulations using only modest resolution. The resolution presented above is typical of each direction in 2D simulations given finite computer resources. This gives us confidence that DADIPIC can correctly predict the anomalous skin effect in more convoluted 2D geometries, where analytic theory cannot be applied.

An idealized 2D ICP reactor that we simulated to observe collisionless heating effects is shown in Fig. 7. The region to the left is the plasma. The electrons are particles while the ions are represented as a uniform, stationary background of positive charge. The same sheath boundary condition as used in the 1D simulations confines the electrons. The four bounding walls of the reactor are conductors. The two internal structures on the right are current driven antennas. The structure between the antennas and the plasma is a dielectric. The driven structures have peak currents in each of 13 A which oscillated at a frequency of 10 MHz. The plasma density is 10^{11} cm^{-3}, and the temperature is 4.65 eV. With $\Delta t = 0.5$ ns and $\Delta x = 0.14$ cm, we have $\omega_{pe}\Delta t = 8.9$ and $\Delta x/\lambda_{De} = 27.6$. These values were chosen after we made short simulations without driven fields which bracketed the numerical energy conserving contour.

Figure 7a shows the structures of the reactor with contours of $E_{y,sol}$ at its maximum superimposed. $E_{y,sol}$ peaks between the driven antennas and falls off due to the conducting walls and the plasma. $E_{y,sol}$ drives a J_y in the plasma as evidenced by the circular pattern of the B-field vectors in Fig. 7b. As with the 1D runs the kinetic energy of the electrons increased due to collisionless heating (Fig. 7c). For these plasma parameters β is 1.65 which gives $\|E_y\|/\|B_z\| = 3.6 \times 10^{-3}$ from the analytic theory. At the center of the dielectric window on the plasma side, $\|E_y\| = 8 \times 10^{-3}$ and $\|B_z\| = 3.3$ which gives $\|E_y\|/\|B_z\| = 2.4 \times 10^{-3}$ showing some effect of the 2D geometry. However, it is the power density into the plasma that is greatly affected in 2D. From analytic theory it is 5.8×10^6 erg/cm^2 s while the measured power divided by the area of the dielectric window gives 4.2×10^5 erg/cm^2 s. The differences occur because of the decrease in E_{sol} near the bounding conducting walls in z and the finite extent of the plasma in x.

An interesting feature of the electron heating in both 1D and 2D is that a significant amount of heating occurs in v_x as well as v_y. In fact, almost all of the heating in the 2D case occurred in the v_x and v_z distributions. Given the small magnitude of E_{sol} in comparison to B_z, the force on a thermal electron due to the B-field is the same order of magnitude as the force due to the E-field. Thus heating in v_y due to E_y is converted to changes in v_x and v_z. In a future publication we shall expand upon these cursory ICP collisionless heating results. For this introduction to the DADIPIC method we have shown the ability of DADIPIC to replicate 1D analytic results and to go beyond such theory to 2D geometries with conducting and dielectric structures.

IV. CONCLUSION AND FUTURE WORK

Darwin direct implicit particle-in-cell (DADIPIC) is a combination of the Darwin and direct implicit methods which eliminates the $c\Delta x/\Delta t < 1$ and $\omega_{pe}\Delta t < 2$ constraints on kinetic plasma simulation. The Darwin method is applied with the streamlined Darwin field (SDF) equations which give the B-field and solenoidal part of the E-field. The SDF equations are solved numerically using coupled equation DADI. The direct implicit method provides an implicit advance of the particles with respect to the electrostatic field. This separation of the field equations has several advantages. The elliptic equations depend only on present particle quantities. Changes in the fields only occur with changes in particle positions and velocities or changes in the boundary conditions. These global field solves tend to decrease the noise in the fields due to the finite number of simulation particles. Boundary conditions also become quite straightforward allowing us to include conducting and dielectric structures in the code. Energy conservation is taken care of by ensuring that the electrostatic fluctuation fields do not cause numerical heating or cooling. The D1 implicit scheme conserves energy for large $\omega_{pe}\Delta t$ and $\Delta x/\lambda_{De}$ as long as $3v_{th}\Delta t/\Delta x \sim 1$.

We presented results for low frequency plasma phenomena showing the ability of DADIPIC to get accurate results with

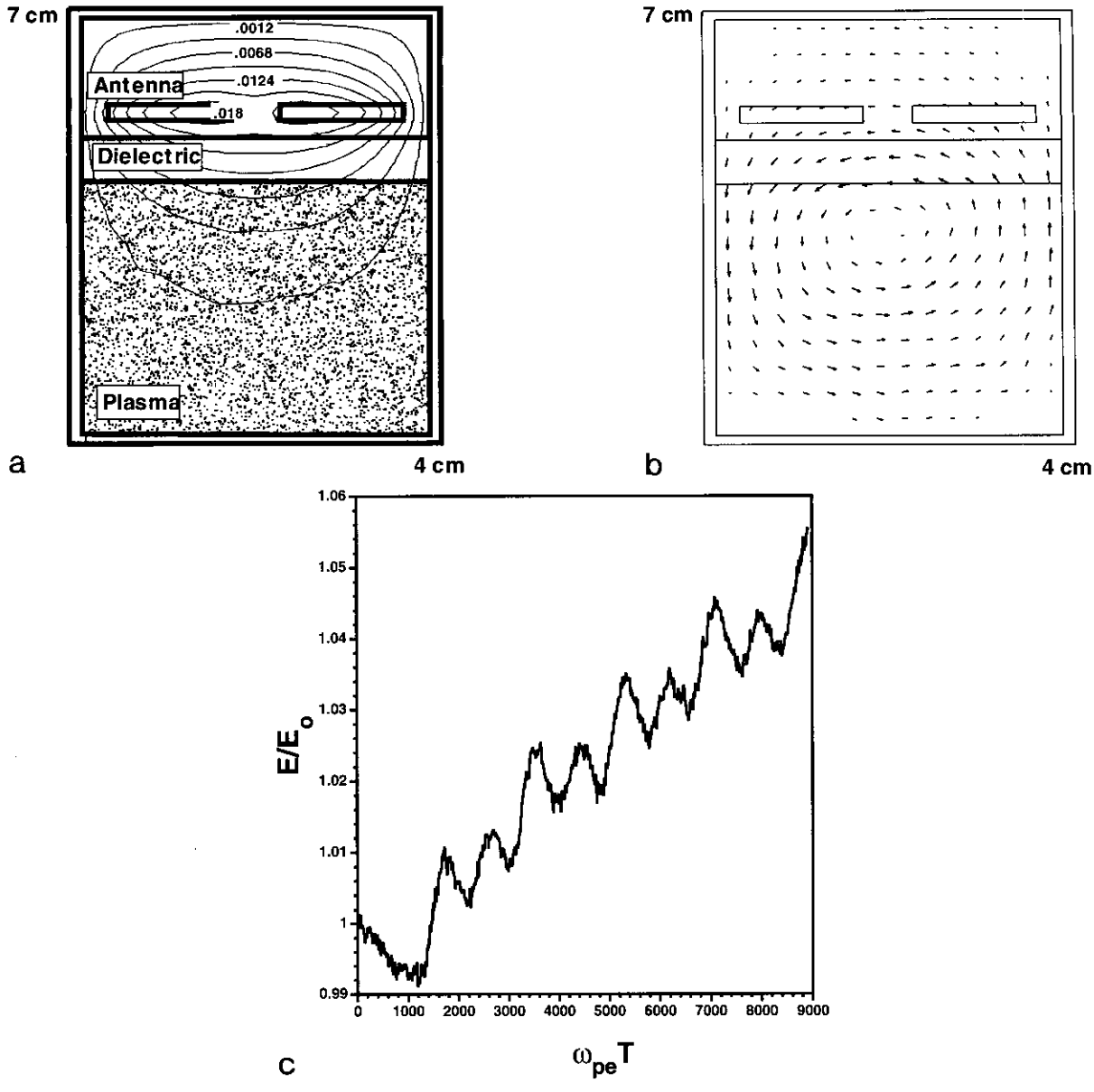

FIG. 7. Results of a 2D ICP simulation (a) particle plot with internal structures and contours of $E_{y,sol}$ at its peak, (b) B-field vector plot at the time of the peak of $E_{y,sol}$, and (c) time history of the particle kinetic energy showing collisionless heating.

large spatial and temporal discretization. Periodic simulations of electron cyclotron waves provided a test of the field solution and particle push routines without the complications of boundary conditions. DADIPIC correctly simulates small amplitude waves as evidenced by the agreement with analytic theory for the form of the fields and the frequency of oscillation. Kinetic phenomena such as damping is also reproduced in agreement with analytic theory as long as there are sufficient numbers of simulation particles to represent the relevant part of the velocity distribution. The second example, collisionless heating in ICPs, highlights the method's capability to model bounded plasmas. The agreement with 1D kinetic theory gives us an idea of the resolution needed for 2D simulations. In 2D we have simulated an idealized plasma processing reactor including a dielectric window and current driven antenna structures. With the algorithm adapted to a code which allows arbitrary 2D structures, DADIPIC has the potential to simulate a wide range of bounded or unbounded low frequency, kinetic plasmas.

In the near term we intend to use DADIPIC in the simulation of ICPs and other collisional bounded plasmas. To accomplish this goal, work is in progress to add capabilities to the present algorithm. Collisions will be added through the use of particle-in-cell with Monte Carlo collisions (PIC-MCC) techniques [33]. We are also developing a boundary condition to model the

unresolved plasma sheaths near bounding walls. In a publication to follow, we shall further expand on spatial and temporal discretization effects on DADIPIC. Our intent here was to present the details of our melding of the Darwin and direct implicit methods: the steps in the time advance of the particles, the field equations to be solved, and the numerical methods used to solve the field equations.

ACKNOWLEDGMENTS

This work would not have been possible without those who have developed the Darwin and direct implicit methods to their present advanced state. In addition we wish to thank D. V. Anderson for help with the CPDES2 routine, D. J. Larson who provided a version of CEDADI, and G. J. DiPeso for numerical techniques and plasma processing discussions. This work was performed under the auspices of the United States Department of Energy by the Lawrence Livermore National Laboratory under Contract W-7405-ENG-48.

REFERENCES

1. A. B. Langdon, B. I. Cohen, and A. Friedman, *J. Comput. Phys.* **51,** 107 (1983).
2. D. W. Hewett and J. K. Boyd, *J. Comput. Phys.* **70,** 166 (1987).
3. D. W. Hewett, G. E. Frances, and C. E. Max, *Phys. Rev. Lett.* **61,** 893 (1988).
4. J. Hopwood, *Plasma Sources Sci. Tech.* **1,** 109 (1992).
5. C. G. Darwin, *Phil. Mag.* **39,** 537 (1920).
6. C. W. Nielson and H. R. Lewis, "Particle-Code Methods in the Nonradiative Limit," in *Methods in Comput. Phys.*, Vol. 16 (Academic Press, New York, 1976).
7. D. W. Hewett, D. J. Larson, and S. Doss, *J. Comput. Phys.* **101,** 11 (1992).
8. A. B. Langdon and D. C. Barnes, *Multiple Time Scales*, Computational Techniques Series (Academic Press, New York, 1985).
9. R. J. Mason, *J. Comput. Phys.* **41,** 233 (1981).
10. J. Denavit, *J. Comput. Phys.* **42,** 337 (1981).
11. J. U. Brackbill and D. W. Forslund, in *Multiple Time Scales*, Computational Techniques Series (Academic Press, New York, 1985).
12. R. J. Mason, in *Multiple Time Scales*, Computational Techniques Series (Academic Press, New York, 1985).
13. B. I. Cohen, A. B. Langdon, and A. Friedman, *J. Comput. Phys.* **56,** 51 (1984).
14. D. W. Hewett and A. B. Langdon, *J. Comput. Phys.* **72,** 121 (1987).
15. M. Tanaka, *J. Comput. Phys.* **107,** 124 (1993).
16. B. I. Cohen, A. B. Langdon, D. W. Hewett, and R. J. Processini, *J. Comput. Phys.* **81,** 151 (1989).
17. C. K. Birdsall and A. B. Langdon, *Plasma Physics via Computer Simulation* (McGraw–Hill, New York, 1985).
18. J. P. Boris, *Proc. Fourth Conf. Numer. Simul. Plasmas, Naval Res. Lab., Washington, DC, November 2–3, 1970*, p. 3.
19. V. Vahedi, Ph.D. thesis, U.C. Berkeley, 1993.
20. G. H. Golub and C. G. Van Loan, *Matrix Computations* (Johns Hopkins Press, Baltimore, 1989).
21. R. Fletcher, in *Numerical Analysis*, Lecture Notes in Mathematics, edited by A. Dold and B. Eckmann (Springer-Verlag, New York, 1975).
22. D. V. Anderson, A. E. Koniges, and D. E. Shumaker, *Comput. Phys. Commun.* **51,** 391 (1988).
23. D. J. Larson, Ph.D. thesis, U. C. Davis, 1992.
24. A. N. Kaufman and P. S. Rostler, *Phys. Fluids* **14,** 446 (1971).
25. Press, Flannery, Teukolsky, and Vetterling, *Numerical Recipies* (Cambridge Univ. Press, New York, 1989).
26. S. Doss and K. Miller, *SIAM J. Numer. Anal.* **16,** 837 (1979).
27. D. W. Hewett and D. J. Larson, LLNL Internal Report, UCRL-UR-110499, 1992 (unpublished).
28. N. A. Krall and A. W. Trivelpiece, *Principles of Plasma Physics* (San Francisco Press, San Francisco, 1986).
29. G. Schmidt, *Physics of High Temperature Plasmas* (Academic Press, New York, 1979).
30. G. E. H. Reuter and E. H. Sondheimer, *Nature* **161,** 336 (1949).
31. D. B. Batchelor, L. A. Berry, E. F. Jaeger, K. C. Shaing, and J. C. Whitson, *Bull. Am. Phys. Soc.* **38,** 2122 (1993).
32. M. M. Turner, *Phys. Rev. Lett.* **71,** 1844 (1993).
33. C. K. Birdsall, *IEEE Trans. Plas. Sci.* **19,** 65 (1991).